CHALMERS
UNIVERSITY OF TECHNOLOGY

All-Metallic-Metasurface-Based Wideband Dual Fabry-Perot Resonance Antenna Array with High Directivity and Polarization Purity

Citation for the original published paper (version of record):
Gomes, B., Uz Zaman, A., Mejia-Salazar, J. (2025). All-Metallic-Metasurface-Based Wideband Dual Fabry-Perot Resonance Antenna Array with High
Directivity and Polarization Purity. IEEE Transactions on Antennas and Propagation, In Press.
http://dx.doi.org/10.1109/TAP.2025.3537688

(article starts on next page)

All-Metallic-Metasurface-Based Wideband Dual Fabry-Perot Resonance Antenna Array with High Directivity and Polarization Purity

Bruno Ferreira Gomes , Ashraf Uz Zaman , J. R. Mejía-Salazar

***Abstract*—In recent years, the integration of metasurface concepts into antenna design has sparked a revolutionary breakthrough, yielding unprecedented advancements in directivity, bandwidth, radiation pattern, polarization, and beam shaping capabilities once thought unachievable. However, further enhancements are still necessary, particularly in terms of integrability and loss reduction, while simultaneously broadening the operational bandwidth and enhancing gain and directivity. In this work, we demonstrate that incorporating the gap-waveguide (GW) technology into the radiator section can be leveraged to improve bandwidth and directivity of antenna arrays, mimicking a dual perfect electric conductor-perfect magnetic conductor Fabry-Perot resonant cavity. Importantly, our concept comprises an entirely metallic 4×4 metasurface-based antenna array, diverging from prior research that employed dielectric components in metasurface design. As a result, the measured bandwidth was around 21% (12 GHz-14.8 GHz) with a measured gain of up to 22.9 dBi. Furthermore, we implement GW technology in the feeding layer, directly coupling it to the radiating layer through slots, thereby optimizing the footprint.**

***Index Terms*—Metasurface, All-metal, Metantennas, Antenna Array, Gap Waveguide**

I. Introduction

Metamaterials and metasurfaces, renowned for their unique and unparalleled electromagnetic properties, are revolutionizing antenna design by overcoming traditional limitations. Conventional antenna design, rooted in decades-old theories, often faces challenges like restricted bandwidth, limited gain, inefficient radiation patterns, and suboptimal efficiency. However, the integration of metasurface concepts with antenna theory is pushing the boundaries of modern antenna engineering [1]–[3]. Recent advancements have showcased the ability of metasurfaces to enable antennas with exceptional performance in directivity, bandwidth, radiation pattern control, polarization, and beam shaping –capabilities previously unattainable using traditional approaches [4]–[7]. Metasurfaces consist of two-dimensional arrays of sub-wavelength scatterers, which allow precise manipulation of electromagnetic fields. This control introduces unparalleled versatility in antenna design [1], [8].

Applications of metasurfaces include transmit-reflect arrays, which function as planar lenses or reflectors with engineered frequency-dependent properties [9]. These structures are practical and accessible, as they can be fabricated using common materials such as metal sheets or printed circuit board (PCB) technology [10]. Additionally, metasurfaces enhance antenna polarization control, enabling transformations such as linear-to-circular or linear-to-slanted polarization conversions [11], [12]. In array designs, metasurfaces placed between antenna elements can mitigate mutual coupling, reducing unwanted resonances and enabling tailored solutions [13]. These designs typically position metasurfaces in the near-field to far-field region of the feeding antenna, providing precise control over radiated waves. However, to refine radiation mechanisms further, metasurfaces can be integrated into the reactive near-field region. This integration governs the antenna's behavior more actively, unlocking new design opportunities.

When metasurfaces are seamlessly incorporated into the radiation mechanism of antennas, they form "metaantennas" [1]–[3]. In metaantennas, metasurfaces enhance key properties such as bandwidth, gain, and radiation pattern behavior while enabling functionalities like circular polarization directly at the element level [14]–[19]. A standout feature of metaantennas is their ability to miniaturize designs, delivering high performance with reduced element size. This leads to improved efficiency, reduced material usage, and cost savings. Hence, metasurfaces can serve either passive or active roles in antenna systems. When placed between the near-field and far-field regions, they act passively, manipulating radiated waves. Conversely, when embedded in the reactive near-field region, metasurfaces actively influence the antenna's radiation mechanism, demonstrating their transformative potential in modern antenna design.

On the other hand, metasurfaces can also be used to enhance the feeding mechanism for antenna elements and arrays, thereby improving bandwidth performance and efficiency. This enhancement contributes to the development of high-quality, low-loss corporate feeding structures [6], [20]. For instance, the gap waveguide (GW) feeding technology [21] was introduced in the last decade to surpass the requirement for electrical contact among different layers of rectangular waveguide array antennas. The GW feeding employs a metasurface that

This work has been partially funded by the project XGM-AFCCT-2024-3-1-1 supported by xGMobile–EMBRAPII–Inatel Competence Center on 5G and 6G Networks, with financial resources from the PPI IoT/Manufatura 4.0 from MCTI grant number 052/2023, signed with EMBRAPII. Authors wish also acknowledge the financial support from the Brazilian agencies National Council for Scientific and Technological Development-CNPq (314671/2021-8) and FAPEMIG (APQ-05305-23). *(Corresponding author: Jorge Ricardo Mejía-Salazar.)*

B. Ferreira-Gomes and Jorge Ricardo Mejía-Salazar are with the National Institute of Telecommunications (Inatel), 37540-000, Santa Rita do Sapucaí, MG, Brazil. (e-mail: bruno.gomes@mtel.inatel.br; jrmejia@inatel.br).

Ashraf Uz Zaman is with the Department of Electrical Engineering, Chalmers University of Technology, 41296 Gothenburg, Sweden (e-mail: zaman@chalmers.se).

mimics a perfect magnetic conductor (PMC) to control the propagation of electromagnetic waves inside the gap between parallel metal plate waveguides [21], [22]. Unlike conventional planar transmission lines like microstrip and coplanar lines, GW boundary conditions prohibit unwanted electromagnetic coupling or leakage, thereby improving energy efficiency. Furthermore, the engineered effective index of the metasurface allows for antennas with reduced dimensions. This concept was a breakthrough that enabled improved integration levels and inspired several new compact planar array antenna designs with low-sidelobes and ultra-widebands, for single and dual-polarized radiation patterns [23]–[25]. Despite these achievements, current GW technologies are limited to using the metasurface only in the feeding section, typically relying on a certain integration allowance to feed a proper radiating element. This often necessitates the use of multilayer schemes to meet the requirements for bandwidth and standing-wave operation [26], making it challenging to achieve higher levels of integration.

In this work, we introduce a novel approach that utilizes a bed of pins to develop a GW feeding mechanism, which is directly coupled to the radiating layer via slots. This technique streamlines the integration of guided-to-radiating electromagnetic mode transitions during antenna fabrication, building upon a method previously demonstrated to be effective in antenna design [22]. A key breakthrough in this work is the use of metasurface-based parallel plate radiating elements. This design creates a structure that simultaneously exhibits two distinct types of cavities: a PEC-PEC cavity, formed by the two flat metallic bases, and a PMC-PMC cavity, defined by the top-to-top distance between the metasurfaces. This novel approach broadens the spectrum of available modes, significantly expanding the antenna's operational bandwidth by simultaneously exciting both electric and magnetic Fabry-Perot resonances within the metasurface-based parallel plate radiator. This advancement not only enhances performance but also positions our concept as a game-changer in the field of metaantenna technology. Moreover, our metasurface-based antenna design is entirely metallic, in contrast to previous designs that integrate dielectric components [27]. This choice is driven by the known reduction in energy efficiency caused by dielectric elements, which suffer from higher dielectric losses. In comparison to recent literature [14]–[19], our concept has several advantages: a more compact design, single-layer feeding, high polarization purity, higher gain levels, broader bandwidths, highly efficient design, and easy-to-scale antenna array [28], [29]. These advantages make our approach ideal for demanding applications, such as Active Electronically Scanned Array (AESA) radars, single-polarized satellite systems, and wireless point-to-point communications. Additionally, the achieved polarization purity can be used to enhance system performance by improving efficiency and capacity, leading to more effective use of the frequency spectrum [30], [31]. Despite the potential bulkiness introduced by the incorporation of parallel plates compared to conventional slot antennas, the trade-off is justified by the superior quality and directive nature of the pencil beam it emits. Notably, our design achieves an impressive gain advantage of approximately 2 dBi per element over standard slot radiating elements, making it compatible with phased array systems. This feature enhances its versatility and opens up new opportunities for innovation in modern antenna design.

II. Antenna Element Design

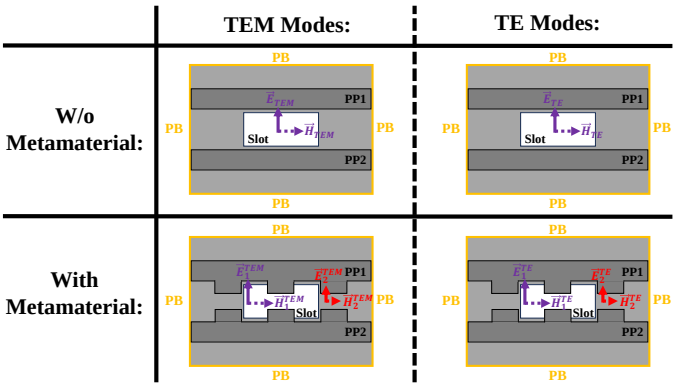

Fig. 1. Pictorial depiction of TEM and TE modes in the systems without (top panel) and with (bottom panel) metasurfaces.

A. Background Concept

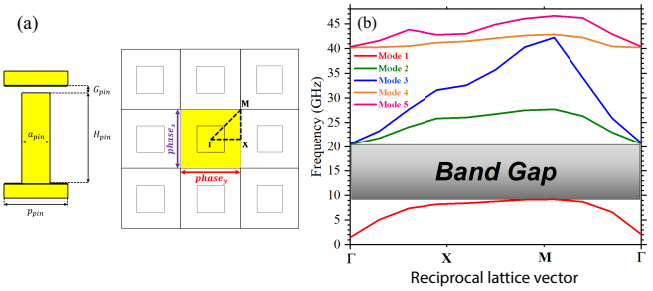

Fig. 2. (a) Schematic representation of a unit cell of the PEC-PMC (i.e., flat metal surface-metal pin based metasurface) cavity and (b) the corresponding PBG profile.

Leveraging the insights from the GW theory [21], [22], we comprehend its essence as an interplay of hard and soft surfaces. This phenomenon typically materializes in waveguides composed of parallel plates with a bed of nails positioned exclusively on one side of the plates, as illustrated (for a single nail) on the left side of Figure 2(a). The plate adorned with the bed of nails serves as a high-impedance surface, emulating a PMC, and is designated as the hard surface. In contrast, the opposing flat metal surface, characterized as a PEC, is labeled the soft surface. In this latter configuration, the propagation of electromagnetic modes is impeded when the distance between the bed of nails and the opposite flat plane is less than a quarter wavelength ($\lambda/4$) at the central frequency. The latter is numerically shown by the photonic bandgap (PBG) in Figure 2(b), calculated for $a_{pin} = 2mm$, $H_{pin} = 6mm$, $G_{pin} = 1mm$, and $p_{pin} = 4.5mm$. These results reveal a Band Gap region (named PBG), which represents a forbidden zone for wave propagation, occurring between 9-20 GHz. Modes outside this range can propagate through the system,

while those within the PBG are blocked. This behavior can be controlled by adjusting the periodicity of the bed of pins in the metasurface, which functions as an artificial PMC, a property not found in naturally occurring materials. Drawing inspiration from this principle, we hypothesize that by incorporating the metasurface concept into both parallel plates, we can intricately tailor and fine-tune the propagation modes through the corresponding PBGs of the periodic structures. In particular, we envision that by implementing this concept into the radiating element, we can effectively enhance the operating bandwidth of a conventional parallel-plate antenna array. It is important to note that, in contrast to GW technology, which utilizes PEC-PMC to suppress propagation, our idea employs a metasurface-metasurface cavity. As demonstrated by the results and subsequent discussions, this cavity simultaneously exhibits both PEC-PEC and PMC-PMC behavior, as will be elaborated upon below.

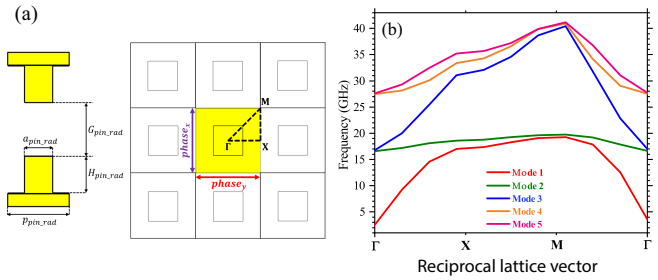

Fig. 3. (a) Illustrative representation of the unit cell of a metasurface-based cavity (i.e., both plates are consist of metallic metasurfaces) and (b) the corresponding PBS.

To elucidate our proposal, we commence with a comparative illustration of the front-view of the radiating element in Figure 1. Two distinct configurations take center stage: one integrates the waveguide concept of parallel plates without (w/o) metasurfaces, and the other incorporates metasurfaces. In both scenarios, the visually represented TEM (transverse electromagnetic) and TE (transverse electric) excitation modes employ a slot as a conduit to efficiently feed the radiating element. For simplicity, and to facilitate the qualitative application of Fabry-Perot resonator (FPR) theory, we initially consider the parallel plates as extending infinitely. In this case, resonances are calculated using the well-established expression [32]

$$f_0 = \frac{nc}{2d}, \quad \text{for} \quad n = 1, 2, 3, \ldots \tag{1}$$

where d denotes the separation between the conductive planes, whilst n and c represent the mode number of the FPR and the speed of light in vacuum, respectively. Conversely, assuming the parallel plates are again infinitely extended but now considering the presence of metasurfaces on both sides of the cavity, the determination of resonant modes hinges on the photonic band structure (PBS) of the system. In this latter case, analytical expressions are elusive, and results can solely be derived through comprehensive full-wave electromagnetic simulations incorporating periodic boundary conditions (PBCs) around the unit cell of the metasurface, as illustrated in Figure 3(a). The numerical data presented in Figure 3(b) correspond precisely to the PBS for the system, calculated for a system with geometrical parameters $a_{\mathrm{pin\_rad}} = 2.2mm$, $G_{\mathrm{pin\_rad}} = 5.1mm$, $p_{\mathrm{pin\_rad}} = 4.9mm$, $H_{\mathrm{pin\_rad}} = 2.95mm$. Importantly, these results reveal the absence of band gaps (BGs), across the entire frequency range. The latter is due to the occurrence of multiple modes in the structure, as it can be seen from the overlap of the operating frequencies for modes 1 to 5 in Figure 3(b).

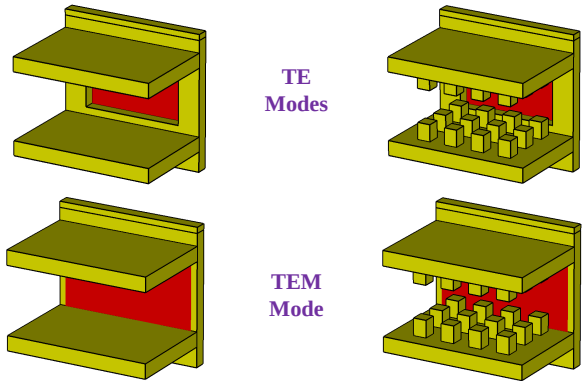

Fig. 4. Depiction of the TE (top panel) and TEM (bottom panel) feeding modes in the systems without (left-hand side) and with (right-hand side) metasurfaces.

The operating frequency band in this work spans from 10 GHz to 18 GHz. The focus of our study transitions to the utilization of the proposed PPs as the radiating elements, as depicted in Figure 4. Initially, we conduct simulations on the PPs, exploring their behavior when fed by TE and TEM modes. This investigation is performed in two scenarios: one without metasurfaces and another with metasurfaces, as illustrated by the top images in Figure 4. The TE modes are introduced into the system through a meticulously designed slot radiating element. In contrast, the TEM modes are directly injected into the PPs region, bypassing consideration of the waveguide modes in the source region. This distinction is visually represented by a larger slot area, highlighted in red, in comparison to the TE modes feeding. Since we are interested in a high-gain antenna array design, periodic boundary conditions (PBCs) are employed along the lateral dimensions of the radiating unit cell in Figure 4. The dimensions of the slots are configured with a width and height of 12.5mm and 8mm, respectively, to have the PP features in a highly compact design. Numerical simulations for the S_{11} parameter are shown in Figures 5(a) and 5(b) for the systems without and with metasurfaces, where results for the TEM and TE modes are presented by solid and dashed lines, respectively. These results are shown for different separations (d) between the PPs.

In Figure 5(a), the TEM mode (depicted by solid lines) within the PPs (without metasurfaces) clearly exhibits a lack of cut-off frequency, showcasing broadband impedance matching above 13GHz. The latter suggests a near-perfect approximation of the wave impedance within the PPs to 377 Ohms, effectively minimizing reflections back to the source and ensuring an efficient radiation process. In contrast, the TE modes (illustrated by dashed lines) guided within the PPs environment experience reflections due to the unmatched wave impedance

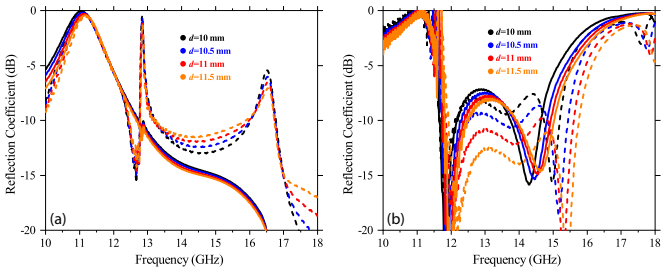

Fig. 5. Results are shown for the system a) without and b) with the bed of pins. Solid and dashed lines are for the TEM and TE ports, respectively. The insets in (a) and (b) are used to indicate that black, blue, red, and orange curves are for $d = 10$ mm, $d = 10.5$ mm, $d = 11$ mm, and $d = 11.5$ mm, respectively.

between the input mode and the PP waveguide. Indeed, the TE modes forced within the PPs experience a robust reflection peak induced by an impedance mismatch around 16.7 GHz. It is noteworthy that both TEM and TE modes exhibit a FP resonance around 13 GHz. This resonance aligns well with Eq. (1) (with $f \in [13\text{ GHz}, 15\text{ GHz}]$ for $d \in [10\text{ mm}, 11.5\text{ mm}]$) for a hypothetical PEC cavity (i.e., considering infinite PEC flat plates). On the other hand, the outcomes in Figure 5(b) unveil the emergence of a higher-frequency resonance for both TEM and TE modes with the addition of metasurfaces on both PPs (illustrated in the right panel of Figure 4). Simultaneously, the initial resonance subtly shifts to a lower frequency (from $\sim$ 13 GHz to $\sim$ 12 GHz). As the bed of nails on both PPs mimics PMCs, the newfound higher-frequency resonance can be regarded as a FP resonance in a PMC cavity (see the Appendix section for further explanations). While there exist analytical expressions for FP resonances in ideal PMC flat cavities [33], we lack the means to derive equations for the effective width, permittivity, and permeability of the emulated PMC cavity with metasurfaces. Therefore, in contrast to Eq. (1), we cannot formulate an equation to delineate the higher-frequency FP resonance in Figure 5(b).

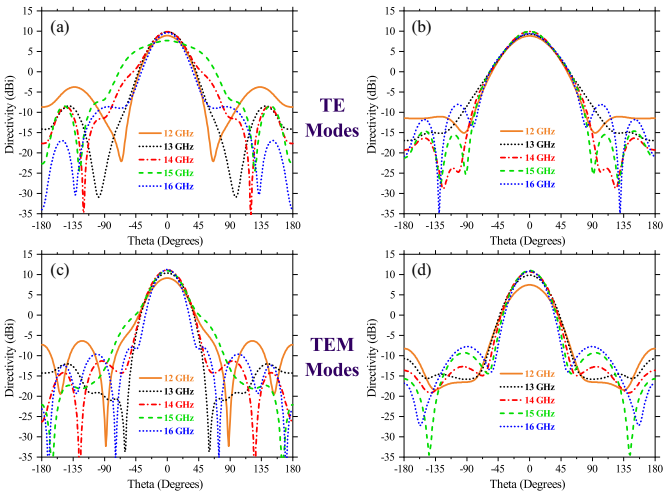

Fig. 6. Far-field radiation patterns for (a)-(b) TE and (c)-(d) TEM modes. Data is comparatively presented for the antenna with pins in (a) and (c), and without pins in (b) and (d). Simulations were carried out for frequencies ranging from 12 GHz to 16 GHz, as shown in the insets.

Despite a slight narrowing of the impedance-matched band (for both polarizations) in the system with metasurfaces, resulting from the effective hybridization of PEC and PMC FP resonances within the radiating element (refer to Figure 5(b)), numerical data in Figures 6(a)-(b) and Figures 6(c)-(d) indicate an enhancement in the system's directivity for TE and TEM modes, respectively. These results are comparatively shown for five different frequencies, namely 12 GHz, 13 GHz, 14 GHz, 15 GHz, within the impedance-matched frequency band. In particular, Figures 6(a)-(c) (Figures 6(b)-(d)) show numerical results for directivity of the radiating element with (w/o) metasurfaces.

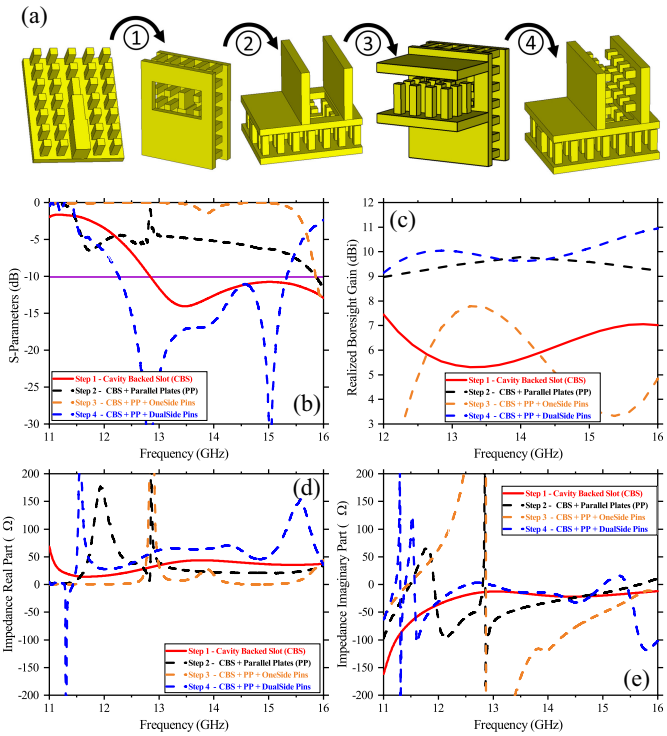

Fig. 7. (a) Successive steps to prototype the antenna in this work: 1) a cavity back slotted (CBS) radiator; 2) CBS + parallel plates resonator; 3) CBS + parallel plates resonator with pins on one side; 4) CBS + parallel plates resonator with pins on both sides. Numerical results from full-wave electromagnetic simulations are shown for the (b) S-Parameters and (b) Boresight gain associated to each one of the prototyping steps in (a).

B. Integrated Gap-Waveguide Parallel Plate Design

Upon finalizing the design of the radiating element, our focus shifted to implementing a gap waveguide transmission line for the feeding mechanism. Specifically, each slot is meticulously connected through a probe, culminating in a cavity-backed slot antenna configuration. A noteworthy aspect is the transition from the probe to the slot, enabling the seamless feeding of parallel plates and resulting in an impressively compact radiating mechanism. The systematic design of the radiating unit cell is illustrated in Figure 7(a). The corresponding S parameters, boresight gains, and impedance (both real and imaginary parts) behavior at each design step are presented in Figures 7(b), 7(c), 7(d), and 7(e), respectively. Notably, in Step 3, the reflection is considerably high due

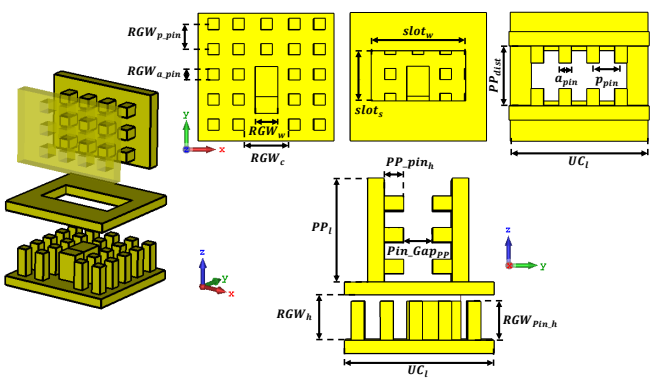

Fig. 8. Parametric view of the antenna radiating element. The design parameters are $RGW_{\mathrm{p\_pin}} = 4.5$ mm, $RGW_{\mathrm{a\_pin}} = 2$ mm, $RGW_{\mathrm{w}} = 4$ mm, $RGW_{\mathrm{c}} = 8$ mm, $slot_{\mathrm{w}} = 17$ mm, $slot_{\mathrm{s}} = 9$ mm, $PP_{\mathrm{dist}} = 10.5$ mm, $a_{\mathrm{pin}} = 2.2$ mm, $p_{\mathrm{pin}} = 4.9$ mm, $UC_{\mathrm{l}} = 23.5$ mm, $PP_{\mathrm{l}} = 16$ mm, $RGW_{\mathrm{h}} = 7$ mm, $PP_{\mathrm{pin\_h}} = 3$ mm, $Pin_{\mathrm{Gap\_PP}} = 4.5$ mm and $RGW_{\mathrm{Pin\_h}} = 6$.

to the soft-hard boundary conditions. These conditions create an environment where the real impedance approaches zero, effectively preventing any mode propagation within the system. In contrast, Step 4 reveals a series of impedance-matched resonances for the two-cavity system, demonstrating a marked improvement in performance. The real and imaginary parts of the impedance curves further illustrate how the multi-resonant scheme can be achieved. When the imaginary part of the impedance is almost zero and fluctuates within the frequency band of interest, the real part can be matched and stabilized around 50 Ohms. Figure 8 showcases the set of geometrical parameters for the designed radiating device, with their corresponding numerical values provided in the caption.

To further elaborate on the dual-cavity aperture behavior, Figure 9 shows the electric field distribution across multiple planes in the radiating section, specifically: 1) Slot XY-plane, 2) XY-plane, 3) XZ-plane, and 4) YZ-plane. This visualization demonstrates how the behavior of these field lines aligns with the generated patterns shown in Figure 6. The feeding section is also included in this overview, illustrating how the main beam and corner refraction contribute to the creation of the radiation pattern. The electric field (E-field) is plotted for two different observation points: when its components are real ($\Phi = 0°$) and when they are imaginary ($\Phi = 90°$). Notably, the E-field distribution at 12 GHz and 15 GHz, as well as at 13 GHz and 14 GHz, shows how the dual-cavity aperture using pins can bring multiple close resonances together, effectively widening the bandwidth of the radiating element. For the 15 GHz E-field distribution, it is evident that the line pattern is broader than at other frequencies, as the field escapes the parallel plate region. This results in a broader radiation pattern and a drop in directivity, which helps to widen the overall radiation pattern.

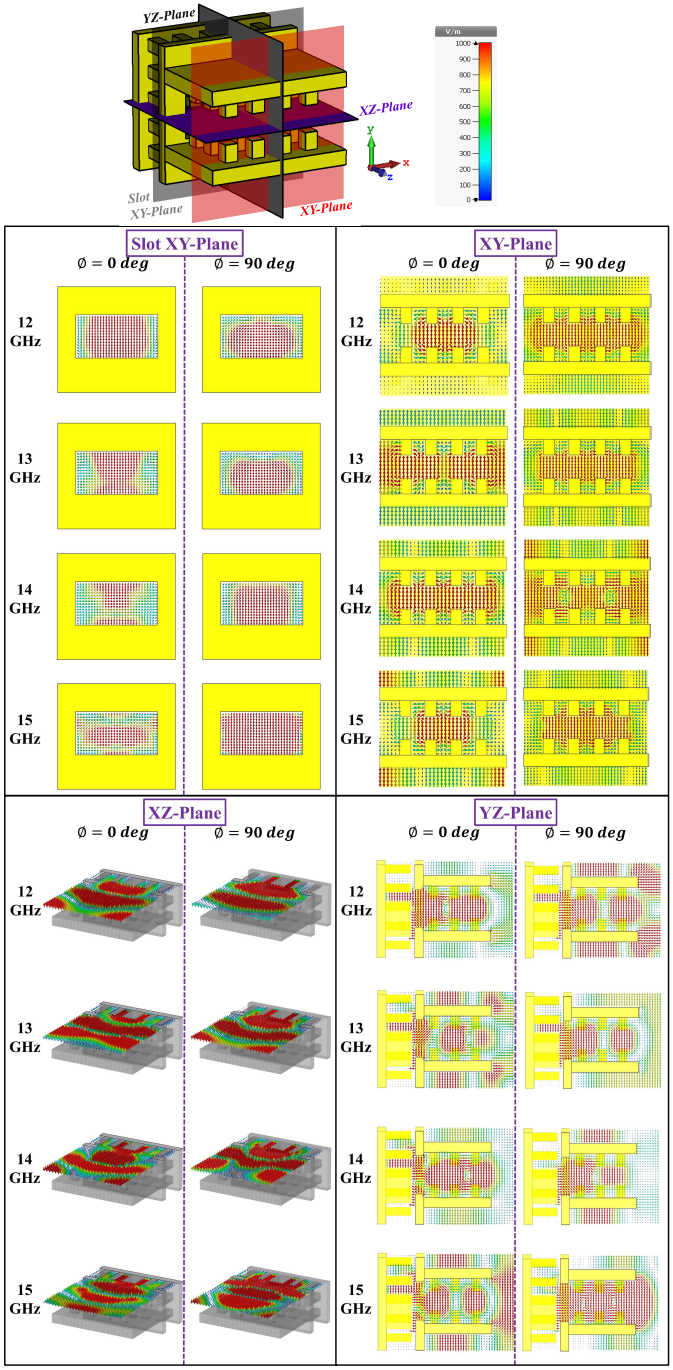

Fig. 9. Numerical results illustrating the variation of the electric field distribution across multiple observation planes within the specified frequency band. Each plane offers a detailed view of how the electric field changes at different positions, providing significant insights into the field's behavior and characteristics over the frequency range.

C. Simulated Results

To enhance understanding of the operational principles, we conducted simulations of the antenna element unit cell across various scenarios through the commercial software CST Microwave Studio. These included a single-element radiating antenna, as well as linear or planar arrays achieved through the implementation of periodic boundaries in one or both directions along the unit cell plane, as illustrated in Figure 10(a). When simulated under periodic boundaries (PBs), the active Voltage Standing Wave Ratio (VSWR) of the unit cell was considered instead of the real element unit cell in the array. Four distinct scenarios were examined in the simulations, as

depicted in Figure 10(a), each labeled according to the utilization of PB and/or OB (open boundaries) boundary conditions. Specifically, the first scenario employed OBs simultaneously along the x- and y-axes (labelled OB all), while the second and third scenarios alternated PBs and OBs along the x (PP-Active) and y (Y-Active) directions, respectively. The fourth scenario involved PBs simultaneously along the x- and y-axes (labelled PB all-Active), as schematized. The corresponding S_{11} parameter was calculated and comparatively plotted in Figure 10(b) for all cases. Additionally, the figures of merit, defined as boresight gain, azimuth half-power beam-width (A-HPBW), and elevation half-power beam-width (E-HPBW), are shown in Figures 11(a) to 11(c), respectively. Analysis of these

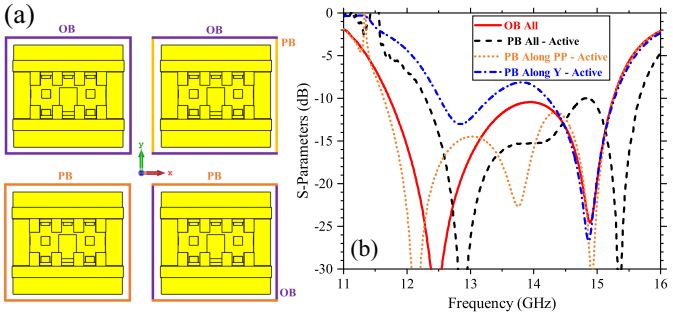

Fig. 10. (a) Description of the simulated element boundary conditions and (b) the related reflection coefficient results under each circumstance.

results reveals that the reflection coefficient reaches 26.24% (11.72 GHz–15.26 GHz) for the first scenario, where the first resonance is broader than the second. This behavior arises from the usage of metasurfaces, which induce the combination of two modes. A deeper understanding of the last phenomenon is facilitated by examining the pattern parameters in Figure 11. Notably, a variation in behavior occurs at approximately 13.5 GHz, causing the mode inside to become more directive, resulting in a broader E-HPBW, which decreases to an average of 50 degrees at 14 GHz. Despite the significant drop in E-HPBW, the increase in A-HPBW suggests the influence of the hidden mode within the broader resonance.

In the second scenario, where PB along PP-Active are considered, we observe the emergence of three resonances. This indicates a split in the broader behavior previously noted. This active case serves as an example of the unit-cell's application in a linear array configuration. The reflection coefficient in this case reaches 27% (11.63 GHz-15.26 GHz). Examining the pattern parameters, it can be noted a stable performance around 8 dBi for boresight gain within the region containing the first two mode resonances. This stability is reflected in a slight decrease in the A-HPBW, which corresponds to the pattern associated with the PB orientation along the PPs. Additionally, we observe a stable variation in the E-HPBW, with a smooth transition from wider to narrower beam widths. These results suggest that the first and second resonances share the same mode nature, indicating that the mode inside remains consistent but with different cut-off frequencies. These modes are generated by both the PP (PEC plates) and the emulated PPs (PMCs plates) created by the pins. Furthermore, an intrinsic resonance occurs within the structure, leading to a drop in the boresight gain at 14.3 GHz, which subsequently broadens the A-HPBW. This is followed by the emergence of a highly directive mode observed at 14.9 GHz, resulting in a severe narrowing of the A-HPBW.

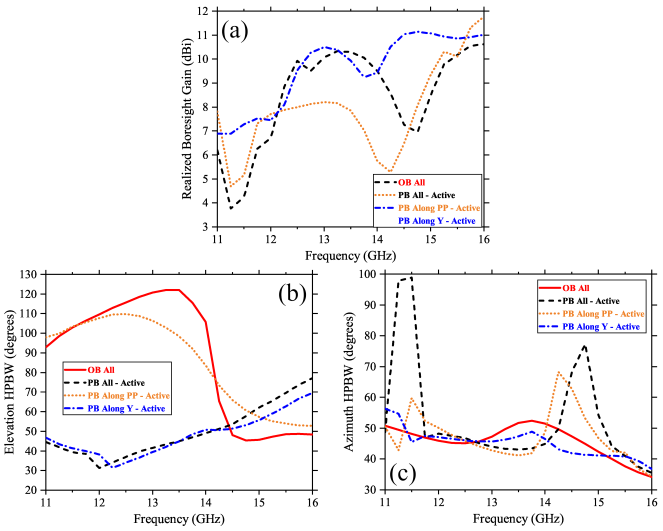

Fig. 11. Evolution of radiation pattern figures-of-merit for the simulated element under varying boundary conditions: (a) boresight gain, (b) A-HPBW, and (c) E-HPBW.

Regarding the third case, which involves the use of PB along Y-Active, we observe a significant impact on the matching of the unit cells, resulting in a notable reduction and suppression of the two modes responsible for the broader first resonance observed previously. However, the second resonance remains strong due to its dominant nature. In this active linear array solution, we note significant changes primarily in the E-HPBW, as the array factor is now related to this axis. The previously observed broad E-HPBW is now reduced within the bandwidth of interest, with variations observed at 12.25 GHz and 14 GHz. Notably, the predominant behavior for the E-HPBW differs from the previously observed pattern, as it gradually broadens over frequency, directly impacting the realized gain, which is significantly improved with this arrayed selection. Furthermore, a higher directivity is observed in the unit cell's behavior. Finally, in the fourth case, we present the solution of the unit cell using PB All-Active, which is particularly significant as it demonstrates the proposed concept when developing a planar array configuration as an antenna. In this specific case, we observe a combination of both the second and third scenarios, which is clearly evident in the pattern parameters and the reflection coefficient. Regarding impedance behavior, we note that the resonances are shifted to higher frequencies due to the unmatched behavior caused in the third case, leading to a slight increase in reflection levels. The achieved bandwidth is 24.2% (12.29 GHz-15.67 GHz), which is still satisfactory, although further impedance transformation will be necessary, specifically for this case when implemented in the antenna. Furthermore, analyzing the pattern parameters, we observe that the tendencies of both the second and third modes are directly evident, indicating similar behavior for the E-HPBW and A-HPBW, with only slight differences. In

the E-HPBW, the significant variation is shifted to 12 GHz, and a more stable performance is achieved in the rest of the bandwidth. For the A-HPBW, there is a tendency toward higher frequencies, reflecting the insertion of elements in the other direction, which modifies the pattern of the wave predominantly polarized in the azimuth/horizontal direction. Additionally, in the boresight gain, we observe that the overall performance aligns with both cases, and the drop at approximately 14 GHz is more pronounced in the combination, which has also shifted to higher frequencies, coinciding with the position of the inner resonance masked in the reflection coefficient.

III. 4x4 Antenna Array Design

A. Feeding Network

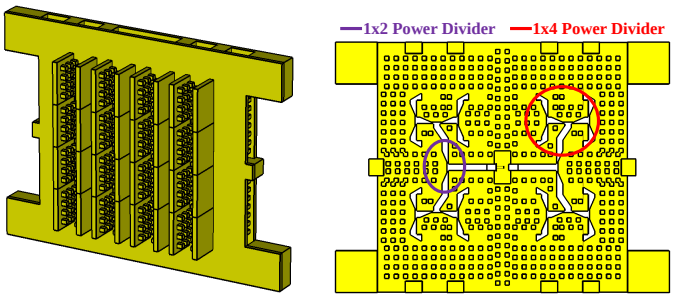

Fig. 12. Viewing of external and internal designed antenna model comprising radiation and signal layers. On left side, the 3D model of the full 4x4 proposed array and on right side, the signal distribution portraying the designed power dividers .

Upon completion and optimization of the antenna element design, we progressed to demonstrate the concept and implementation by integrating the element into a planar antenna array configured as a 4×4 array. Given that the antenna element already encompasses feeding and matching integration, our challenge shifted to designing a complex feeding network capable of providing each element with the necessary phases and amplitudes. To enhance the feeding technique and align with the input port of the antenna element, we also employed the concept of gap waveguide to construct the entire feeding network. Our aim was to feed all elements with maximum accuracy in amplitude and phase to ensure a beam pointing towards the boresight direction. Achieving this required minimizing discrepancies in amplitudes and phases across all elements. In Figure 12, we present a 3D schematic of the final 4×4 planar array. The left side illustrates the complete scheme, while the right side showcases the gap waveguide feeding network with the Rad PP and top GND (Ground Plane) removed for demonstration purposes. For the planar array environment, we chose an element-to-element spacing of 22.5 mm, approximately corresponding to λ_0 at the center of the operating frequency range. Given that parallel plate designs utilizing an all-metal concept typically result in unit cell sizes comparable to the wavelength, careful attention was paid to minimize the generation of grating lobes. Optimal element spacing was sought to balance and optimize the parallel plates, ensuring lower grating lobes and minimizing array side-lobe levels (SLL). Developing these complex feeding networks posed challenges in achieving wideband behavior covering the entire antenna element operating bandwidth while maintaining stable performance in amplitude and phase across each element. To address this, each transition and component of the feeding network was optimized to minimize reflection coefficients and ensure stable transmission coefficients. Power dividers required careful optimization, employing techniques such as tapered transitions to produce smooth impedance transformation. By cascading each component of the feeding network with low input reflections, we achieved a high-quality feeding network capable of effectively feeding the radiating component.

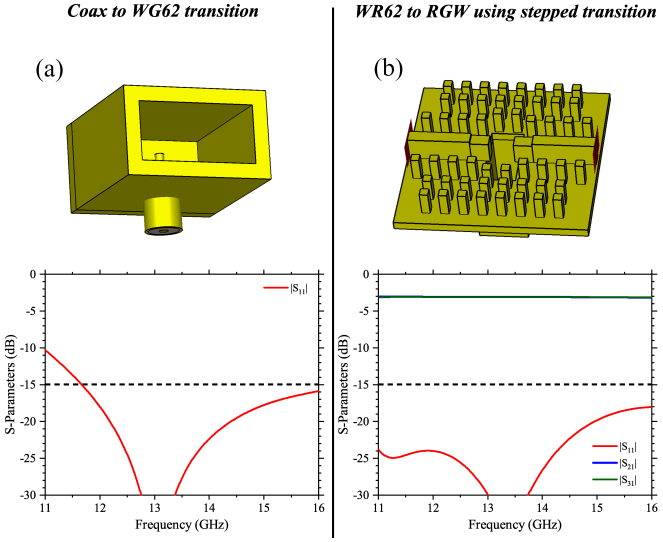

Fig. 13. Reflection parameters of the optimized transitions: (a) coax-to-WR62 waveguide transition and (b) WR62-to-groove gap waveguide transition, both engineered to maintain reflection levels below -15 dB across the entire impedance bandwidth.

In Figure 13, we showcase the initial two steps of the feeding network. Figure 13(a) shows the coax to WR62 waveguide transition, featuring inner dimensions of 15.8 mm×7.9 mm. This component serves as a prototype user interface for post-manufacture device measurement. While this transition offers a degree of wideband capability, it is constrained by waveguide cut-off modes, leading to limitations in reflection levels. We optimized this component to achieve reflection levels of at least -15 dB across the entire impedance bandwidth, as it can be seen from numerical results in Figure 13(a). On the other hand, Figure 13(b) shows a transition from WR62 to groove gap waveguide, implemented as a vertical power divider. A stepped transitions was used to facilitate impedance transformation and ensure efficient power flow throughout the feeding network, optimizing its performance. The top ground layer is hidden in the schematic to clearly show our idea. The objective for this component was to achieve reflection coefficient levels of at least -20 dB, as shown by numerical data in Figure 13(b). By vertically dividing power as per the proposed method, we ensure that the phases of each port differ

by 180 degrees. Within the gap waveguide layer, the pins were optimized to establish the correct bandgap, facilitating the flow of modes within the desired bandwidth. The last process follows the mechanism demonstrated in Figure 2, where the dispersion diagram is plotted across the entire Brillouin zone. The bandgap was precisely engineered within the 9 GHz to 20.5 GHz bandwidth to enable precise feeding of the radiator element, as discussed earlier.

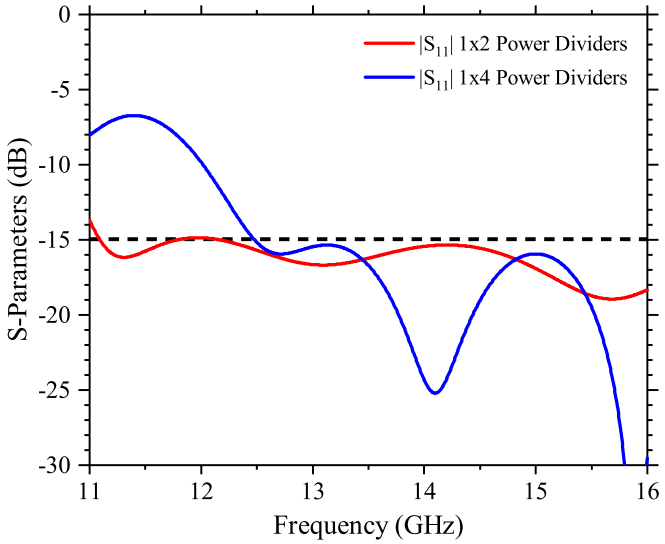

Fig. 14. Reflection coefficient simulated results for the different designed power dividers located in the GW signal layer.

To delve into the performance of the feeding network, reference should be made to Figure 12, where the 1×2 and 1×4 power dividers are highlighted. To maintain broad bandwidth while minimizing reflection, we applied a standard transformation with tapered behavior. In the 1×4 divider, two sequential transformations were necessary due to element proximity, making it more critical for compactness. Additionally, a groove tilt was introduced to enhance compactness, albeit causing slight power distribution imbalance among the elements. Despite this, the design remains compact and aligns with element spacing sizes. Figure 14 illustrates the reflection coefficient performance for both dividers. The 1×2 divider demonstrates stability below -15 dB across the entire bandwidth. Conversely, the 1×4 exhibits improved performance above 12.5 GHz, achieving reflections below -15 dB. Further optimization post-divider integration enhanced system performance, evident in subsequent full antenna simulations. It's noteworthy that to mitigate the 180–degree phase imbalance introduced by the central vertical power divider in the gap waveguide layer, the 1×4 dividers were mirrored concerning the array's center, enabling compensation for this phase shift in both slots and parallel plates.

B. Prototype Fabrication

The prototype, shown in Figure 15, was crafted using a CNC (Computer Numerical Control) milling machine. To ensure ease of assembly and meet the mechanical requirements for prototyping, the radiator PP with metamaterial pins was

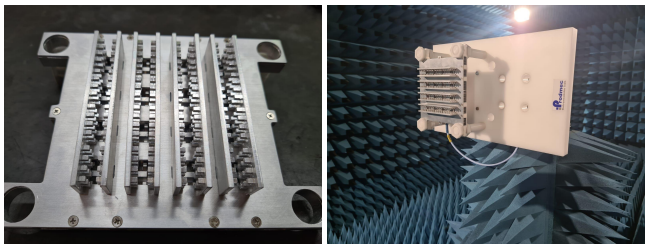

Fig. 15. Prototype viewing of the proposed antenna. Top view with the radiation aperture and 3D-view in the anechoic chamber ready for measurements.

fabricated in separate sections. The design includes a minimum distance of 0.6λ at the center frequency between the edges of the PPs and the antenna edges. This additional area on the antenna prototype was verified to have no adverse effect on the simulated or measured gain levels. Moreover, it contributed to improved side lobe performance, attributed to current dissipation around this extended region. However, challenges arose during the prototyping phase, particularly regarding the assembly of these components. Unlike conventional PP designs, which are typically manufactured as single units, our approach necessitated separate production to incorporate the metamaterial pins. Consequently, precisely inserting these PPs into the horizontal GND plane at a precise 90-degree vertical orientation proved to be a significant challenge, requiring meticulous attention to detail to minimize errors. Another noteworthy issue was the necessity of securely affixing these PPs within the horizontal top GND. To address this, a solution was devised involving the creation of a smaller slot in the top GND and a corresponding tooth-like structure on the PPs. This enabled a snug fit between the two components, with the teeth being hammered into the slot to ensure a secure connection. However, a drawback of this solution was the need for the slot to be slightly larger than the teeth, resulting in small unfilled areas between the components. This discrepancy led to minor current instabilities in the vicinity, particularly notable due to the presence of the ridge gap waveguide in the layer below. Despite the high precision achieved during the prototyping process, this solution contributed to resonance shifts, as demonstrated in Figure 16. Notably, the red circles highlight imperfections in the fit between the teeth and the slot, underscoring the impact of fabrication errors on performance. Future endeavors can explore various avenues to address fabrication errors in the radiating component. For instance, one viable approach entails applying conductive glue in the affected regions, thereby reducing the slot area and alleviating the current discontinuity issue. Alternatively, fabricating the entire piece from a single aluminum block using a 3D-axis CNC machine offers another promising solution. While less conventional, this method could enable precise cutting of the block in every axis, yielding a final piece of exceptional accuracy.

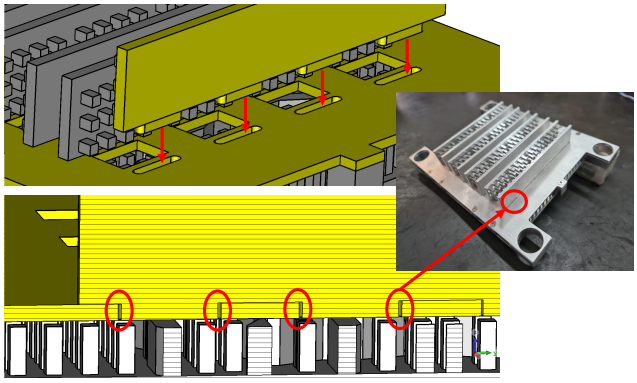

Fig. 16. Demonstration of the situational concern in regards of the mounting method of the prototype, related to the divergence in the measured parameters.

IV. Antenna Array Simulated and Measured Results

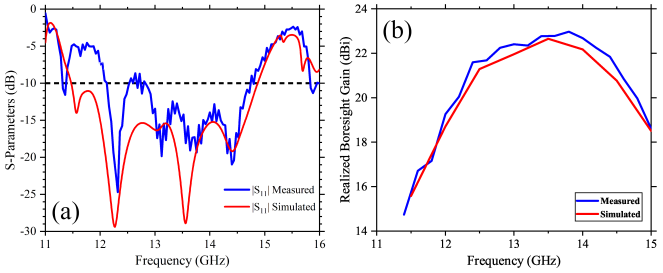

Fig. 17. Comparison between simulated and measured S-parameters and Realized Boresight Gain of the proposed antenna concept.

A comparison between the simulated and measured results of the manufactured antenna array prototype is presented in Figures 17(a)-(b). The simulated reflection coefficient achieves an operational bandwidth of 26.1% considering VSWR<2 (see Figure 17(a)), whereas the measured result achieved 20.9%. It is worth noting that while the behavior of the resonances could be accurately predicted, fabrication errors and tolerances caused some resonances to shift slightly in frequency (as previously discussed), directly impacting the narrowing of the measured impedance bandwidth. Simulated and measured boresight gain varied between 15.2 dBi and 22.9 dBi (see Figure 17(b)). The high directivity of the antenna elements used in the array contributes to overall device performance, resulting in a more stable and high-gain pencil-beam. Minor discrepancies between simulated and measured results are apparent, largely attributable to the all-metal design principle. These findings highlight the feasibility of our concept in designing highly efficient, compact, and directional antennas with minimal energy loss. Specifically, the averaged radiation efficiency reached approximately 97.5%, while the total efficiency averaged 96% across the entire operational bandwidth.

Normalized radiation patterns at 12 GHz, 13 GHz, and 14 GHz are shown in Figures 18(a)-(f), showcasing the high accuracy of predicted co-polarization radiation patterns. The measured SLL for these specific patterns were -10.5 dB, -13.8 dB, and -11.9 dB for the $\phi = 0$ cut-plane, and

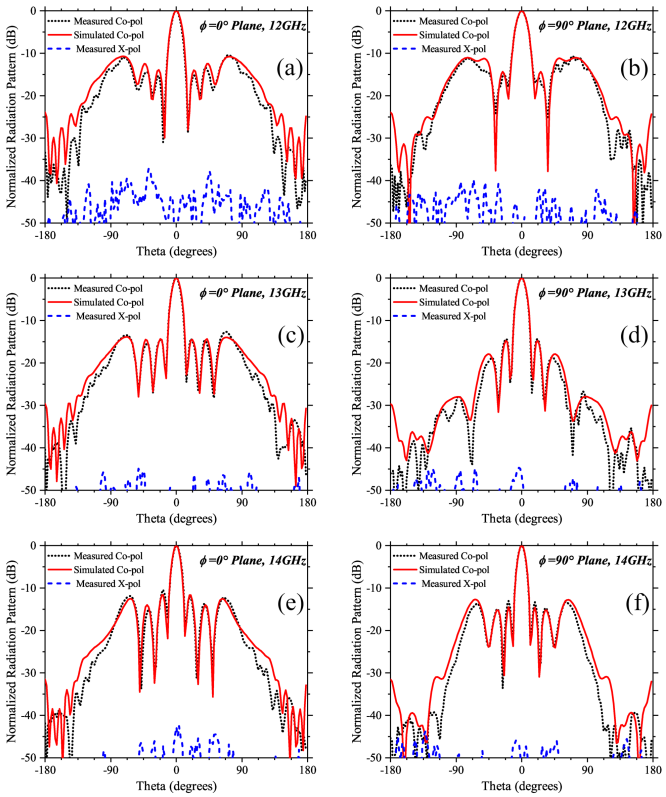

Fig. 18. Comparison between simulated and measured radiation patterns for both farfield cut sections: azimuth and elevation, demonstrated at different frequency points.

-11.2 dB, -15.1 dB, and -12.9 dB for the $\phi = 90$ cut-plane, respectively.

V. Analysis and Contrast with the State-of-the-Art Design Concepts

The Cross Polarization Ratio (CPR) serves as a quantification of the dominance of the co-polar pattern over the cross-polar pattern at specific azimuth and elevation angles. Essentially, it acts as a metric for assessing the linear polarization purity of an antenna prototype, with higher CPR values indicating greater purity. In an ideal scenario, such as with a theoretical rectangular slot antenna, cross-polarization values are expected to be minimal, resulting in a high CPR, which is indicative of high polarization purity. However, practical constraints often limit our ability to precisely measure these extremely low levels of cross-polarization. Environmental factors, including scattering within the measurement chamber, can contribute to increased cross-pol values, sometimes averaging around -30 dB. This phenomenon was observed in our study, where despite the anticipated high polarization purity facilitated by the slot and parallel plate design, cross-pol values averaged around -45 dB at boresight. Nonetheless, this outcome still signifies a high CPR, highlighting the antenna's capability to maintain polarization purity under real-world measurement conditions. Additionally, we compared our proposed idea with previously reported antennas utilizing metal technology and integrated metamaterial-based solutions. The performance of

TABLE I
COMPARISON OF PERFORMANCE WITH OTHER METAL ANTENNAS WITH GW FEEDING NETWORK

Designs	Frequency Band (GHz)	Array Size	Number of Layers	Imp. BW (%)	Gain (dBi)
Ref. [34]	23-30.5	8x8	2	28	20.5-26.4
Ref. [35]	56-65.7	16x16	2	16	>32.5
Ref. [36]	18.8-30.3	8x8	2	46.8	24.3-27.7
Ref. [37]	12-15	2x2	1	21	12.2-13.8
This work	12-14.8	4x4	1	20.5	15.2-22.9

TABLE II
COMPARISON OF PERFORMANCE WITH OTHER METAANTENNAS

Designs	Frequency (GHz)	Array Size	Feeding Technology	Imp. BW (%)	Peak Gain (dBi)	Apperture Efficiency (%)
Ref. [38]	60	8x8	SIW	15.4	24.9	<49.4
Ref. [39]	5.5	Single Element	Microstrip Line	24.5	7.8	Not Calculated
Ref. [40]	34	4x4	SIGW	35.5	17.4	<30.2
Ref. [41]	3.5	2x2	Microstrip Line	17.8	11.9	<45.3
This work	13.5	4x4	RGW	20.5	22.9	<89

various antenna characterization parameters is summarized in Tables I and II.

Upon comparing with the references listed in Table I, it becomes apparent that despite the increased size of the prototype –achieving an aperture volume of 90 mm $\times$ 90 mm $\times$ 27.5 mm and ensuring a maximum aperture efficiency of 89% (the external area designated for mechanical support, as previously mentioned, was included in the calculations)– the impedance bandwidth could be maintained at a comparable level. Furthermore, the realized boresight gain related to the array can be increased, owing to the nature of the elements used. An advantageous aspect of this solution is its integration into a single-layer design, which effectively reduces the complexity of development. From Table II, it is evident that the concept presented in this work achieves superior aperture efficiency compared to other metantennas. This superiority arises from the conventional use of PCB technology in state-of-the-art metantennas, emphasizing the absence of all-metal-based metantenna concepts in antenna array engineering.

VI. CONCLUSIONS

Summarizing, this work presents a novel methodology for crafting highly integrable antenna array designs utilizing all-metallic metasurfaces. A key innovation lies in integrating metasurfaces directly into the radiating element to improve the impedance-matching, resulting in approximately 21% (12 GHz-14.8 GHz) bandwidth. Specifically, we introduce a mechanism akin to GW technology into the radiating element, which, as validated through numerical simulations and experimental measurements, yields a dual cavity exhibiting characteristics of both a PMC and a PEC, thereby showcasing electric and magnetic Fabry-Perot resonances. Importantly, this bandwidth expansion is achieved without compromising the high polarization purity expected from parallel plate-based antennas, as corroborated by experimental evidence. Furthermore, by integrating GW technology into both the feeding layer and the radiating metasurface-based parallel plates, we realize a highly compact all-metallic design boasting broad bandwidth, high gain (22.9 dBi), high polarization purity, and a stable radiation pattern.

APPENDIX

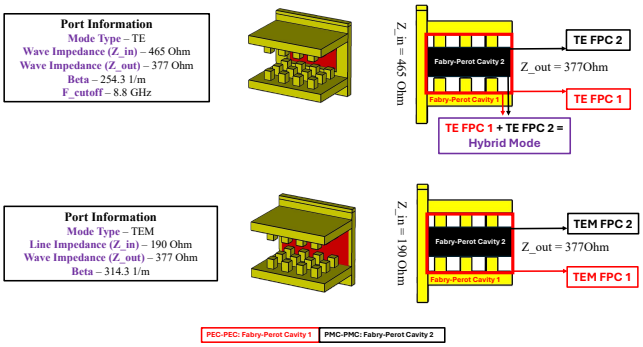

Fig. 19. Schematic representation of PEC-PEC and PMC-PMC cavities and their modes for TE and TEM excitation ports in the proposed metasurface-based radiating element. Numerical parameters for the TE and TEM modes are shown in the rectangular boxes on left-side panels.

In the simplest scenario of an ideal parallel plate waveguide of infinite extent, wave solutions are well-established. While the TEM mode does not exhibit a cut-off frequency, the TE and TM modes feature a cut-off frequency determined by Eq. (1), which depends on the boundary conditions. In practical, non-ideal scenarios –where the waveguide is finite and directly fed via a probe (e.g., a slot)– the system also exhibits resonant behavior characteristic of a Fabry-Perot resonant cavity. This behavior is leveraged in our concept to enhance the operating bandwidth. For numerical analysis of the proposed radiation mechanism, the system is directly fed by an emulated probe supporting both TEM and TE modes. The port and environmental configurations are presented in the rectangular box on the left panel of Figure 19. Without a metasurface, the system operates as a conventional Fabry-Perot cavity, governed by PEC-PEC boundary conditions, in agreement with established literature. In contrast, introducing a metasurface transforms the system into a dual-cavity configuration, as depicted on the

right panel of Figure 19. This configuration combines the original PEC-PEC boundaries (highlighted with an open red rectangle) with a newly created PMC-PMC cavity (indicated by a solid black rectangle). The PMC-PMC cavity arises from the collective electromagnetic response of the periodic metallic pins forming the metasurface, which significantly modifies the waveguide's resonant characteristics and expands its operational capabilities. For more precise numerical analyses to unveil the relationship between the simulated modes in Figures 5 and the cavities explained in Figures 19, we see the resonances for the TE mode:

- TE FPC1 produces a 12 GHz resonance,
- TE FPC2 produces a 15.2 GHz resonance, and
- A hybridized mode (TE FPC Hybrid) occurs at 14 GHz, situated between TE FPC1 and TE FPC2,

whilst results for the TEM mode produce

- TEM FPC1 produces a 12 GHz resonance, and
- TEM FPC2 produces a 14.5 GHz resonance,

which are in good agreement with numerical results for the entire prototype.

REFERENCES

[1] C. Z. . Q. X. Liu, W.E.I., "Dispersion-engineered wideband low-profile metasurface antennas," *Front Inform Technol Electron Eng*, vol. 21, pp. 27–38, 2020.

[2] J. Wang, Y. Li, Z. H. Jiang, T. Shi, M.-C. Tang, Z. Zhou, Z. N. Chen, and C.-W. Qiu, "Metantenna: When metasurface meets antenna again," *IEEE Transactions on Antennas and Propagation*, vol. 68, no. 3, pp. 1332–1347, 2020.

[3] Z. N. Chen, Q. Lou, and W. Liu, "Metantennas: Opportunities and challenges in future microwave metasurface antenna research and applications," in *2022 16th European Conference on Antennas and Propagation (EuCAP)*, 2022, pp. 1–5.

[4] J.-W. Lian, M. Ansari, P. Hu, Y. J. Guo, and D. Ding, "Wideband and high-efficiency parallel-plate luneburg lens employing all-metal metamaterial for multibeam antenna applications," *IEEE Transactions on Antennas and Propagation*, vol. 71, no. 4, pp. 3193–3203, 2023.

[5] F. Ahmed, M. U. Afzal, T. Hayat, K. P. Esselle, and D. N. Thalakotuna, "A near-field meta-steering antenna system with fully metallic metasurfaces," *IEEE Transactions on Antennas and Propagation*, vol. 70, no. 11, pp. 10 062–10 075, 2022.

[6] T. E. J. U. Z. YONG, "Antenna array based on one or more metamaterial structures," U.S. Patent US20220109246A1, June 2022.

[7] D. Chen, W. Yang, W. Che, and Q. Xue, "Broadband stable-gain multiresonance antenna using nonperiodic square-ring metasurface," *IEEE Antennas and Wireless Propagation Letters*, vol. 18, no. 8, pp. 1537–1541, 2019.

[8] F. Mesa, G. Valerio, R. Rodríguez-Berral, and O. Quevedo-Teruel, "Simulation-assisted efficient computation of the dispersion diagram of periodic structures: A comprehensive overview with applications to filters, leaky-wave antennas and metasurfaces," *IEEE Antennas and Propagation Magazine*, vol. 63, no. 5, pp. 33–45, 2021.

[9] Z. H. Jiang, Y. Zhang, J. Xu, Y. Yu, and W. Hong, "Integrated broadband circularly polarized multibeam antennas using berry-phase transmit-arrays for ka -band applications," *IEEE Transactions on Antennas and Propagation*, vol. 68, no. 2, pp. 859–872, 2020.

[10] O. Yesilyurt and G. Turhan-Sayan, "Metasurface lens for ultra-wideband planar antenna," *IEEE Transactions on Antennas and Propagation*, vol. 68, no. 2, pp. 719–726, 2020.

[11] N. Yogesh and Z. Ouyang, *Metamaterial Frequency Selective Surfaces As Polarizers*. Singapore: Springer Nature Singapore, 2020, pp. 1–28. [Online]. Available: https://doi.org/10.1007/978-981-15-8597-5_10-1

[12] Z. Lin, X. Li, and S. He, "High-performance silicon te-pass polarizer assisted by anisotropic metamaterials," *Opt. Express*, vol. 30, no. 14, pp. 24 841–24 851, Jul 2022. [Online]. Available: https://opg.optica.org/oe/abstract.cfm?URI=oe-30-14-24841

[13] M. Alibakhshikenari, M. Khalily, B. S. Virdee, C. H. See, R. A. Abd-Alhameed, and E. Limiti, "Mutual-coupling isolation using embedded metamaterial em bandgap decoupling slab for densely packed array antennas," *IEEE Access*, vol. 7, pp. 51 827–51 840, 2019.

[14] N.-S. Nie, X.-S. Yang, Z. N. Chen, and B.-Z. Wang, "A low-profile wideband hybrid metasurface antenna array for 5g and wifi systems," *IEEE Transactions on Antennas and Propagation*, vol. 68, no. 2, pp. 665–671, 2020.

[15] T. Li and Z. N. Chen, "Shared-surface dual-band antenna for 5g applications," *IEEE Transactions on Antennas and Propagation*, vol. 68, no. 2, pp. 1128–1133, 2020.

[16] J.-W. Lian, D. Ding, and R. Chen, "Wideband millimeter-wave substrate-integrated waveguide-fed metasurface antenna," *IEEE Transactions on Antennas and Propagation*, vol. 70, no. 7, pp. 5335–5344, 2022.

[17] W. E. I. Liu, Z. N. Chen, and X. Qing, "Broadband low-profile l-probe fed metasurface antenna with tm leaky wave and te surface wave resonances," *IEEE Transactions on Antennas and Propagation*, vol. 68, no. 3, pp. 1348–1355, 2020.

[18] M. Y. Jamal, M. Li, K. L. Yeung, X. Li, L. Jiang, and T. Itoh, "A low-profile fabry–pérot cavity antenna using anisotropic metasurface," *IEEE Antennas and Wireless Propagation Letters*, vol. 21, no. 2, pp. 356–360, 2022.

[19] J. d. Dieu Ntawangaheza, L. Sun, S. Wang, Y. Li, Z. Zheng, D. Biao, and G. Rushingabigwi, "A single-layer low-profile broadband metasurface-inspired antenna with monopole-like radiation characteristics," *IEEE Transactions on Antennas and Propagation*, vol. 70, no. 6, pp. 4818–4823, 2022.

[20] E. R.-I. E. A. P.-S. Kildal, A.U. Zaman and A. Valero-Nogueira, *IET Microwaves, Antennas & Propagation*, vol. 5, pp. 262–270(8), February 2011. [Online]. Available: https://digital-library.theiet.org/content/journals/10.1049/iet-map.2010.0089

[21] P.-S. Kildal, E. Alfonso, A. Valero-Nogueira, and E. Rajo-Iglesias, "Local metamaterial-based waveguides in gaps between parallel metal plates," *IEEE Antennas and Wireless Propagation Letters*, vol. 8, pp. 84–87, 2009.

[22] E. Rajo-Iglesias, M. Ferrando-Rocher, and A. U. Zaman, "Gap waveguide technology for millimeter-wave antenna systems," *IEEE Communications Magazine*, vol. 56, no. 7, pp. 14–20, 2018.

[23] M. Ferrando-Rocher, J. I. Herranz-Herruzo, A. Valero-Nogueira, B. Bernardo-Clemente, A. U. Zaman, and J. Yang, "8×8 ka-band dual-polarized array antenna based on gap waveguide technology," *IEEE Transactions on Antennas and Propagation*, vol. 67, no. 7, pp. 4579–4588, 2019.

[24] T. Zhang, R. Tang, L. Chen, S. Yang, X. Liu, and J. Yang, "Ultra-wideband full-metal planar array antenna with a combination of ridge gap waveguide and e-plane groove gap waveguide," *IEEE Transactions on Antennas and Propagation*, vol. 70, no. 9, pp. 8051–8058, 2022.

[25] J. Yue, C. Zhou, K. Xiao, L. Ding, and S. Chai, "W-band low-sidelobe series-fed slot array antenna based on groove gap waveguide," *IEEE Antennas and Wireless Propagation Letters*, vol. 22, no. 4, pp. 908–912, 2023.

[26] M. Ferrando-Rocher, A. Valero-Nogueira, J. I. Herranz-Herruzo, A. Berenguer, and B. Bernardo-Clemente, "Groove gap waveguides: A contactless solution for multilayer slotted-waveguide array antenna assembly," in *2016 10th European Conference on Antennas and Propagation (EuCAP)*, 2016, pp. 1–4.

[27] D. Chen, Q. Xue, W. Yang, K.-S. Chin, H. Jin, and W. Che, "A compact wideband low-profile metasurface antenna loaded with patch-via-wall structure," *IEEE Antennas and Wireless Propagation Letters*, vol. 22, no. 1, pp. 179–183, 2023.

[28] K. Zhang, P. J. Soh, T. Wu, M. Wang, and S. Yan, "A compact multimode antenna design based on metasurface for wideband applications," *IEEE Transactions on Antennas and Propagation*, vol. 72, no. 8, pp. 6747–6752, 2024.

[29] D. Yang, Z. N. Chen, J. Yin, and P. Liu, "Mode conversion for broadband mutual coupling suppression of a slot-fed metasurface mosaic antenna," *IEEE Transactions on Antennas and Propagation*, vol. 72, no. 9, pp. 6930–6938, 2024.

[30] D. R. Prado, M. Arrebola, M. R. Pino, and G. Goussetis, "Broadband reflectarray with high polarization purity for 4k and 8k uhdtv dvb-s2," *IEEE Access*, vol. 8, pp. 100 712–100 720, 2020.

[31] Anywaves, "The importance of signal polarization in satellite communications," 2024, https://anywaves.com/resources/blog/definition-whats-polarization-for-space-antennas-and-why-is-it-important [Accessed: 10th November 2024].

[32] K. Lu, Y. Ding, and K. W. Leung, "A new fabry-perot resonator antenna fed by an l-probe," *IEEE Transactions on Antennas and Propagation*, vol. 60, no. 3, pp. 1237–1244, 2012.
[33] K. F. Renk, *Fabry–Perot Resonator*. Berlin, Heidelberg: Springer Berlin Heidelberg, 2012, pp. 43–54. [Online]. Available: https://doi.org/10.1007/978-3-642-23565-8_3
[34] W. Y. Yong, A. Haddadi, T. Emanuelsson, and A. A. Glazunov, "A bandwidth-enhanced cavity-backed slot array antenna for mmwave fixed-beam applications," *IEEE Antennas and Wireless Propagation Letters*, vol. 19, no. 11, pp. 1924–1928, 2020.
[35] D. Zarifi, A. Farahbakhsh, A. U. Zaman, and P.-S. Kildal, "Design and fabrication of a high-gain 60-ghz corrugated slot antenna array with ridge gap waveguide distribution layer," *IEEE Transactions on Antennas and Propagation*, vol. 64, no. 7, pp. 2905–2913, 2016.
[36] T. Zhang, R. Tang, L. Chen, S. Yang, X. Liu, and J. Yang, "Ultra-wideband full-metal planar array antenna with a combination of ridge gap waveguide and e-plane groove gap waveguide," *IEEE Transactions on Antennas and Propagation*, vol. 70, no. 9, pp. 8051–8058, 2022.
[37] A. U. Zaman and P.-S. Kildal, "Wide-band slot antenna arrays with single-layer corporate-feed network in ridge gap waveguide technology," *IEEE Transactions on Antennas and Propagation*, vol. 62, no. 6, pp. 2992–3001, 2014.
[38] W. Liu, Z. N. Chen, and X. Qing, "60-ghz thin broadband high-gain ltcc metamaterial-mushroom antenna array," *IEEE Transactions on Antennas and Propagation*, vol. 62, no. 9, pp. 4592–4601, 2014.
[39] W. E. I. Liu, Z. N. Chen, X. Qing, J. Shi, and F. H. Lin, "Miniaturized wideband metasurface antennas," *IEEE Transactions on Antennas and Propagation*, vol. 65, no. 12, pp. 7345–7349, 2017.
[40] T. Li and Z. N. Chen, "Wideband sidelobe-level reduced ka -band metasurface antenna array fed by substrate-integrated gap waveguide using characteristic mode analysis," *IEEE Transactions on Antennas and Propagation*, vol. 68, no. 3, pp. 1356–1365, 2020.
[41] J. F. Gao and F. H. Lin, "Modeling and analysis of wideband multilayer metasurface antenna array using characteristic-mode analysis," *IEEE Transactions on Antennas and Propagation*, vol. 71, no. 3, pp. 2832–2836, 2023.

Bruno Ferreira Gomes in Santa Rita do Sapucaí, MG, Brazil. He received his B.Sc. in Telecommunications Engineering from the National Institute of Telecommunications (INATEL), Brazil, and Jade Hochschule University of Applied Sciences, Germany, both in 2019. He completed his M.Sc. at INATEL in 2024. Since 2021, he has worked in the industry as an antenna design engineer for base station antennas, specializing in the design of radiating elements and antenna array development. His research interests include wideband and ultrawideband linearly and circularly polarized antennas, high-gain high-efficient dual-polarized antenna arrays, metamaterials and metasurface-driven antennas, gap waveguide technology, electromagnetic transparent structures, and multiband antennas.

Ashraf Uz Zaman (SM'22) was born in Chittagong, Bangladesh. He received the B.Sc. in Electrical & Electronic Engineering from CUET in 2000. Then he completed his M.Sc. and Ph.D. degrees from the Chalmers University of Technology, Gothenburg, Sweden, in 2007 and 2013, respectively. He is currently an Associate Professor with the Communication and Antenna Systems Division, Chalmers University of Technology, Sweden. His current research interests include high gain millimeter-wave planar antennas, gap waveguide technology, frequency-selective surfaces, quasi-optical beamformers, microwave passive components, RF packaging techniques and low-loss integration of MMICs with the antennas etc. Now, he is the director of mmWave and THz antenna measurement lab at Chalmers and he is leading a research group consisting of 6 PhD students, 3 MSc. thesis students and one Postdoc research fellow. He is also co-founder of a startup company named Gapwaves AB. He is the inventor of 7 granted patents.

Jorge Ricardo Mejía-Salazar obtained his B.Sc., M.Sc., and Ph.D. degrees in Physics from Universidad del Valle in Cali, Colombia, in 2008, 2009, and 2014, respectively. After completing his Ph.D., he pursued postdoctoral research at the Institute of Physics, Federal University of Alagoas, Maceió, Brazil (2014–2016), and later at the Sao Carlos Institute of Physics, University of Sao Paulo, Brazil (2016–2018). Since 2018, Jorge has been a Professor at the National Institute of Telecommunications (Inatel) in Santa Rita do Sapucaí, Minas Gerais, Brazil. His research interests include applied electromagnetism, reconfigurable intelligent surfaces (RIS), antennas, nanoantennas, and the electromagnetic principles governing chiral, magneto-chiral, magneto-optic, and magnetoplasmonic effects in nanostructures.